nature communications

Article

https://doi.org/10.1038/s41467-025-67678-5

Lithium-ion battery recycling through an integrated electro-membrane crystallization technology

Received: 25 April 2025

Accepted: 5 December 2025

Published online: 20 December 2025

Check for updates

Yan Zhao[1,2,12] ✉, Yangbo Qiu[1,12], Lei Xia[3,12], Xi Zhang[4,5], Shuang Zheng[1], Gang Lu[6], Jin Shang[7], Raf Dewil[8,9], Seth B. Darling[4,5], Bart Van der Bruggen[2,10,11] ✉ & Chuyang Tang[1] ✉

Lithium-ion battery (LIB) recycling is crucial for energy security, environmental sustainability, and economic viability, as the finite lifespan of LIBs results in a significant annual accumulation of spent units. However, effectively and precisely recovering valuable metal ions such as Li^+, Mn^{2+}, Ni^{2+} and Co^{2+} from complex LIB leaching solutions remains a major challenge. Here, we present a scalable electro-membrane crystallization-assisted general recycling (e-MCGR) technology for the selective and efficient recovery of those metal ions from LIB leaching solutions. By synergistically integrating electrochemical and electro-membrane technologies, our proposed technology incorporates four key configurations: selective membrane dual-stage distillation, bipolar membrane in-situ crystallization, membrane metal-complexing ex-situ crystallization, and membrane metal-extracting temporal crystallization. We systematically analyze the metal-ion transfer kinetics of electro-membranes (ion selectivity and permeation rates) and the performance of electro-membrane crystallization systems (recovery rates and product purity), alongside evaluating energy consumption, economic viability, and environmental benefits. Our optimized e-MCGR process achieves a recovery of 95.5% for Li^+, 99.5% for Mn^{2+}, 83.1% for Ni^{2+}, and 87.3% for Co^{2+}, yielding high product purities of 99.9% for Li_2CO_3, 99.9% for Mn_3O_4, 99.5% for $Ni(OH)_2$ and 92.5% for $Co(OH)_2$. The e-MCGR technology demonstrates significant potential to reshape LIB recycling paradigms, aligning technological efficiency with energy, environmental and economic sustainability.

Lithium-ion batteries (LIBs), the powerhouse of modern electronics, have been a global cornerstone to power billions of electronic devices[1]. They have undergone exponential and fast development in adding resilience to electrical grids with increasing contributions from intermittent sources[2,3]. By 2024, global LIB production reached approximately 3950 gigawatt-hours (GWh), with China contributing over 2677 GWh of this output, which represented over 65% of the global market share (Fig. 1a). Such rapid expansion of the LIB production underscores China's success in reducing reliance on carbon-based energy while advancing renewable energy adoption (Supplementary Fig. 1). Unfortunately, the finite lifespan of these batteries (typically 2–9 years, around 500–3000 cycles) results in a substantial annual accumulation of spent batteries[4]. According to the data, the global generation of spent LIBs surged 1700 Kilotons (Kt) in 2024, with the volumes expected to rise further as demand grows (Supplementary Fig. 3). This escalating influx

A full list of affiliations appears at the end of the paper. ✉e-mail: yanzhaox@hku.hk; bart.vanderbruggen@kuleuven.be; tangc@hku.hk

of spent batteries poses critical energy, economic, and environmental challenges, particularly in major economies with high LIB usage, such as China, the United States, European nations, Japan, and Korea (Fig. 1b and Supplementary Fig. 2).

The efficient recycling of spent batteries has become an imperative priority[5–7]. Among the complex composition of spent LIBs, the recovery of high-value metal ions, such as Li^+, Mn^{2+}, Ni^{2+}, and Co^{2+}, offers a potential opportunity for resource reclamation[8,9]. Typically, spent LIBs are dissolved in acidic solutions, followed by pH adjustment to obtain a leaching solution[10], from which metal ions need to be recovered efficiently and precisely. To address these challenges, various approaches such as adsorption, ion exchange, solvent extraction, precipitation, or evaporative crystallization have been explored[11–14]. While some of these methods enable metal ion recovery, their limitations stem from imprecise separation and inefficient purification[15,16]. Thus, achieving metal ion recovery with both high recovery and high-purity products in a sustainable manner remains a significant hurdle. Additionally, most existing approaches focus narrowly on technical aspects, often overlooking system-level integration and sustainability[17–19].

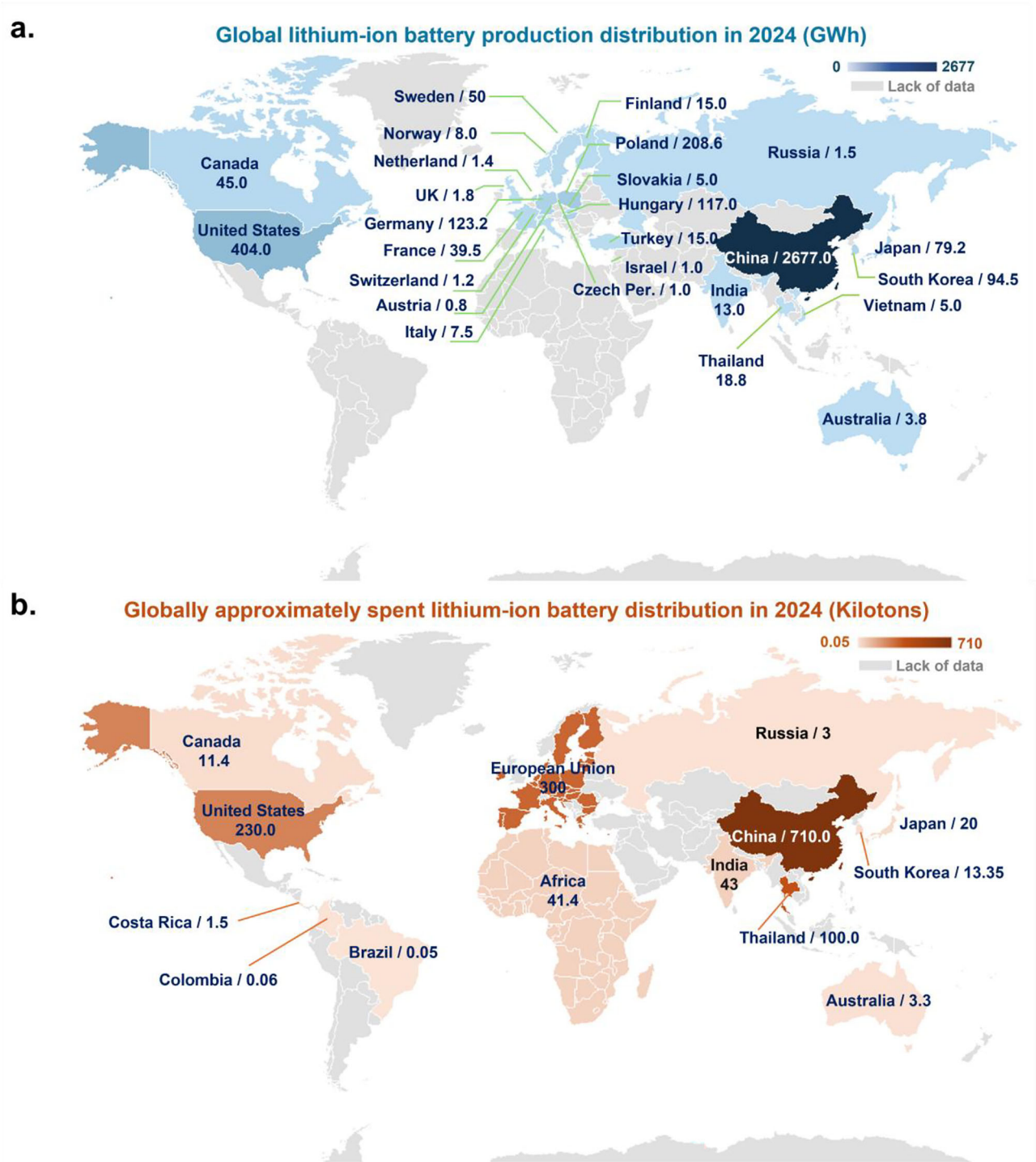

Fig. 1 | Global overview of lithium-ion battery development in 2024. a Global lithium-ion battery production breakdown by region in 2024 (GWh), a visual representation of regional contributions to global lithium-ion battery (LIB) manufacturing, measured in gigawatt-hours (GWh); **b** Global distribution of spent lithium-ion batteries in 2024 (Kilotons). The corresponding references are provided in Supplementary Tables 2 and 4.

In recent decades, membrane technologies with tunable structures and functional groups have shown great promise as an efficient method for ion separation[20–22]. Among them, electrodialysis, by using electro-membranes, has emerged as a viable approach for recovering ion resources from diverse streams[23–25]. Advances in material science have led to the development of electro-membranes with tailored ion selectivity, enabling precise targeting of specific ions even in the presence of competing species with similar physicochemical properties[26–30]. However, ion transport across the electro-membranes is constrained by their ion-transfer kinetics (e-MK), resulting in trade-offs between ion selectivity and permeation rates[13,31–33]. Notably, recent research efforts have been directed toward combining electrochemical systems with crystallization to enhance metal ion recovery, resulting in the development of electrochemical crystallization. This approach enables simultaneous metal ion separation and crystal product generation[24,34–36]. Yet, a trade-off between the high ion recovery rate and product purity exists at the process scale[37–39]. To address this, hybridizing electrochemical systems with electro-membrane technology and crystallization technology (e-MC) offers a promising pathway for achieving metal ions with both high recoveries and high product purities. Previously, membrane technologies have relied on principles such as size exclusion, electrostatic interactions, and chemical affinity to achieve ion selectivity[31,40–42]. Although substantial progress has been made toward developing membranes with precise single-ion selectivity, their utility in real-world resource recovery remains limited by material constraints and has largely been tested only in isolated/single systems[43–45]. Furthermore, their applicability in LIB recycling has not been convincingly demonstrated[42,46].

To bridge this gap, we propose an e-MC-assisted general recycling (e-MCGR) concept, which integrates mature membranes into a closed-loop and modular framework tailored for spent LIB recycling. The e-MCGR concept is designed to address both separation precision and practical applicability while maintaining high recovery and product purity. As illustrated in Fig. 2, the process begins with disassembly and acidic dissolution of spent LIBs, followed by pH adjustment (~7) to generate a representative leaching solution[47]. Valuable metals ions, such as Li^+, Mn^{2+}, Ni^{2+} and Co^{2+}, are then selectively recovered through a three-part process: (i) separation of monovalent cations (Li^+ and Na^+) from divalent cations (Mn^{2+}, Ni^{2+} and Co^{2+}) through selective membrane dual-stage distillation; (ii), separation of monovalent cations from each other (separation Li^+ and Na^+) and Li^+ crystallization via bipolar membrane in situ crystallization and (iii) selective recovery of Mn^{2+}, Ni^{2+} and Co^{2+} by membrane metal-complexing ex situ crystallization and membrane metal-extracting temporal crystallization. These processes enable the recovery of high-purity Li_2CO_3, Mn_3O_4, $Ni(OH)_2$, and $Co(OH)_2$. Despite the strategic importance of metal ion recovery from spent LIBs, no comprehensive study or design has yet explored a fully sustainable LIB recycling through this e-MCGR concept. Furthermore, the potential of LIB recycling to enhance energy security, environmental sustainability, and economic viability remains insufficiently explored. This

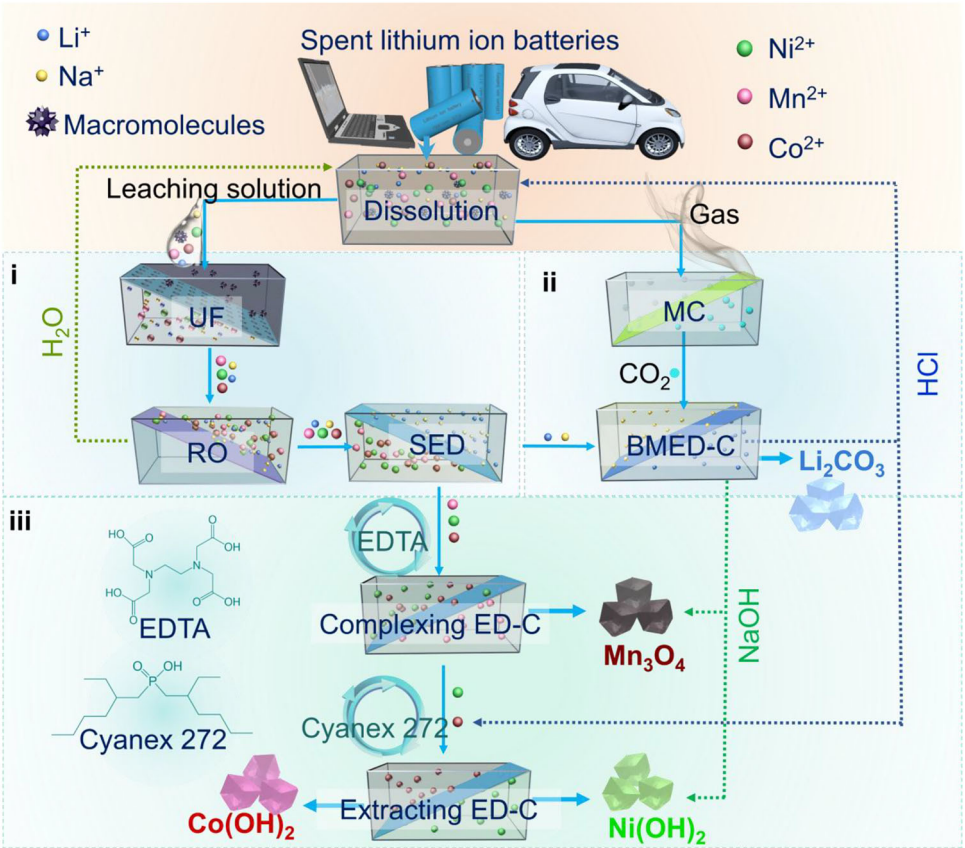

Fig. 2 | Schematic of sustainable lithium-ion battery recycling process based on the concept of the e-MCGR with the design of multiple e-MC configurations by utilizing existing mature membranes. i separation of monovalent cations (Li^+ and Na^+) from divalent cations (Mn^{2+}, Ni^{2+} and Co^{2+}) by using the selective membrane dual-stage distillation technology. UF: ultrafiltration. RO reverse osmosis. SED monovalent selective electrodialysis; **ii** separation of Li^+ from Na^+ via bipolar membrane in situ crystallization technology, and enabling the recovery of high-purity Li_2CO_3. MC membrane contactor. BMED-C bipolar membrane crystallization; **iii** separation of divalent cations from each other (i.e., Mn^{2+}, Ni^{2+}, and Co^{2+}) through the membrane metal-complexing ex situ crystallization (Complexing ED-C) as well as membrane metal-extracting temporal crystallization technology (Extracting ED-C), where Mn^{2+} is separated from Ni^{2+} and Co^{2+} via metal-complexing ex situ crystallization configuration, yielding high-purity Mn_3O_4, followed by Ni^{2+} separation from Co^{2+} via membrane metal-extracting temporal crystallization configuration, producing high-purity $Ni(OH)_2$ and $Co(OH)_2$, respectively. Details of the concept of e-MCGR are provided in Supplementary Fig. 4.

e-MCGR presents an innovative framework and practical strategy for optimizing metal ion recovery, thereby addressing the challenges encountered in sustainable resource recovery from LIBs. Given the global scale of LIB development, this e-MCGR concept and approach contribute a holistic, scalable, and sustainable solution to address global challenges in LIB waste management and resource recovery.

Results

Separation of monovalent cations from divalent cations

The e-MCGR starts with ultrafiltration (UF, Supplementary Table 5), where the organic pollutants in the feed are removed to minimize membrane clogging. Then the metal ions in the feed are concentrated using reverse osmosis (RO, Supplementary Table 6) before entering the ED cell due to low metal ion concentration in spent LIB leaching solutions (Fig. 2, Supplementary Table 7). Due to the unique thermodynamic and physical characteristics of metal ions, such as specific hydrated diameters and hydration energy (Supplementary Table 8), monovalent metal ions (Li^+ and Na^+) can be separated from multivalent metal ions (Mn^{2+}, Ni^{2+}, and Co^{2+}). Recent advancements have enabled the use of commercial monovalent ion-selective electro-membranes, which operate based on mechanisms such as size exclusion and electrostatic repulsion (Fig. 3a and Supplementary Fig. 5). To efficiently recover those valuable metal ions, Li^+ and Na^+ are separated from Mn^{2+}, Ni^{2+}, and Co^{2+} through continuous selective electrodialysis. The separation is firstly evidenced by the change in color of the leaching solution (Fig. 3b), where the dark brown of the leaching solution is changed to a dark red solution containing Mn^{2+}, Ni^{2+}, and Co^{2+}, while the solution containing only Li^+ and Na^+ is colorless.

To enhance separation efficiency, a multi-stage selective electrodialysis could be employed, but it is limited by practical constraints in metal ion recovery rates and the trade-offs in energy, economic, and environmental benefits[48]. Therefore, a more suitable two-stage selective electrodialysis configuration is designed here, termed as selective membrane dual-stage distillation (Supplementary Fig. 6). The impact of current density on e-MK is evaluated by using three current densities (i.e., 1.0, 2.5, and 5.0 mA cm^{-2}). In the first-stage selective electrodialysis at operating condition of 1.0 mA cm^{-2} with 4 L of leaching solutions in the feed chamber, the concentrations of Li^+ and Na^+ increase in the recovery chamber (Fig. 3c). In this configuration, multivalent metal ions (Mn^{2+}, Ni^{2+}, and Co^{2+}) are rejected by the selective membranes, while Li^+ and Na^+ readily permeate (Supplementary Fig. 7). However, residual Mn^{2+} (0.06 g L^{-1}), Ni^{2+} (0.06 g L^{-1}) and Co^{2+} (0.07 g L^{-1}) mixed with amounts of Na^+ (0.04 g L^{-1}) and Li^+ (0.14 g L^{-1}) in transitional chambers necessitate further separation due to the limited selectivity of commercial membranes. Thus, the 2 L transitional solutions (in transitional chamber-1 and transitional chamber-2) from the first-stage selective electrodialysis are fed into the second-stage selective electrodialysis for additional separation (Fig. 3d). This selective membrane dual-stage distillation configuration proves optimal for separating Li^+ and Na^+ from Mn^{2+}, Ni^{2+}, and Co^{2+}. With the combination of first-stage operating at 1 mA cm^{-2} and second-stage at 0.5 mA cm^{-2}, this dual-stage distillation achieves the highest accumulative recoveries of 96.5% for Li^+ and 96.4% for Na^+, while completely rejecting Mn^{2+}, Ni^{2+}, and Co^{2+} (Fig. 3e and Supplementary Fig. 8).

Effectively, the transport of metal ions from the feed chamber to the recovery chamber is governed by e-MK and reflected by voltage change (Supplementary Fig. 9). Regardless of stages or operating conditions, the e-MK is the critical factor for determining metal ion selectivity, permeation rate, and ultimately, recovery and purity. Although additional stages could enhance metal ion recovery purity, they lead to higher losses of Li^+ and Na^+ in the transitional chamber and higher energy consumption. Thus, the selective membrane dual-stage distillation technology strikes an optimal balance for separating monovalent cations (Li^+ and Na^+) and multivalent cations (Mn^{2+}, Ni^{2+}, and Co^{2+}) with current membrane technologies.

A comprehensive evaluation of energy consumption, economic profitability, and environmental benefits is conducted for this selective membrane dual-stage distillation configuration (Supplementary Fig. 10). With this optimized configuration, most of this energy is consumed by metal ion transport in membranes. For this selective membrane dual-stage distillation, key metrics, such as energy consumption (EC), energy cost (C_e), investment cost (C_i), Li^+ recovery cost (C_{Li}), monovalent metal ion recovery rate (R_m), and purity of recovered Li^+ (P_{Li}), are analyzed and summarized (Supplementary Fig. 10 and Supplementary Table 9). For the first-stage selective electrodialysis, the impact of current density on separation kinetics is evaluated at 1.0, 2.5, and 5.0 mA cm^{-2}. At 1.0 mA cm^{-2}, the system demonstrated the lowest energy cost (1.24 \$ kg^{-1}), investment cost (3.78 \$ kg^{-1}), and the energy consumption (11.83 kWh kg^{-1}), along with the highest monovalent cation recovery rate (87.7%), compared to 66.8% and 60.5% at 2.5 and 5.0 mA cm^{-2}, respectively (Fig. 3f). To further enhance Li^+ recovery, transitional solutions from the first-stage selective electrodialysis are processed in a second-stage selective electrodialysis operated at a lower current density (0.5 mA cm^{-2}). Based on the operating conditions and the expenditure per 1 kg of LiCl recovery, this configuration achieves around 96.5% recovery of monovalent metal ions (Li^+ and Na^+), with an energy cost of 2.73 \$ kg^{-1}, investment cost of 13.25 \$ kg^{-1}, and energy consumption of 15.97 kWh kg^{-1} (Fig. 3g). This initial separation of monovalent and multivalent cations is essential for efficient resource recovery, both technologically and in terms of energy, economic, and environmental reasons. While selective membrane dual-stage distillation technology achieves a high separation efficiency, current commercial membranes are limited by their metal ion throughput. In addition, they suffer from severe membrane scaling (Supplementary Figs. 11 and 12). On the one hand, this scaling can be attributed to the inherent poor anti-scaling properties of commercial electro-membrane. On the other hand, water splitting may occur on the CIMS surface as most divalent ions are electrostatically repelled and cannot serve as current carriers. The resulting shortage of charge carriers induces forced dissociation of water into H^+ and OH^-, with OH^- reacting with accumulated metal ions to form insoluble hydroxide precursors that deposit on the membrane surface (Supplementary Fig. 13).

Recovery of Li^+ and Na^+

Following the initial separation configuration, the recovered feed contains only monovalent metal ions (Li^+ and Na^+), yet the lack of highly Li^+-selective electro-membranes poses a significant challenge, and current electrodialysis cannot achieve crystallization. Our innovative approach offers a solution that enables simultaneous metal ion separation and crystallization of Li_2CO_3. Typically, CO_2 is captured by reacting with OH^-, a method commonly employed for carbon capture and storage, and utilized as a carbonate source. Leveraging the bipolar membrane electrodialysis, an in situ crystallization configuration is developed to separate Li^+ from Na^+ while generating high-purity Li_2CO_3 crystals (Supplementary Fig. 14). In this system, CO_2 is captured via a membrane contactor (Supplementary Fig. 15) and reacts with the OH^- generated in situ by the bipolar membrane (chemical reaction pathways are detailed in Supplementary Fig. 16). This hybridization of bipolar membrane and in situ crystallization technologies ensures Li^+ capture, CO_2 utilization, and Li_2CO_3 production (Fig. 4a and Supplementary Fig. 17).

Figure 4b illustrates the mechanisms of the bipolar membrane in situ crystallization process, culminating in the formation of white powder products. Scanning electron microscopy (SEM) reveals that the precipitated powders exhibit a regular octahedral crystal structure with an average diameter of 4 μm (Fig. 4c and Supplementary Fig. 18). The element mapping confirms the homogeneous distribution of C and O within the particles (Supplementary Fig. 18). X-ray photoelectron spectroscopy (XPS) further vindicates the crystal purity and shows atomic

https://doi.org/10.1038/s41467-025-67678-5

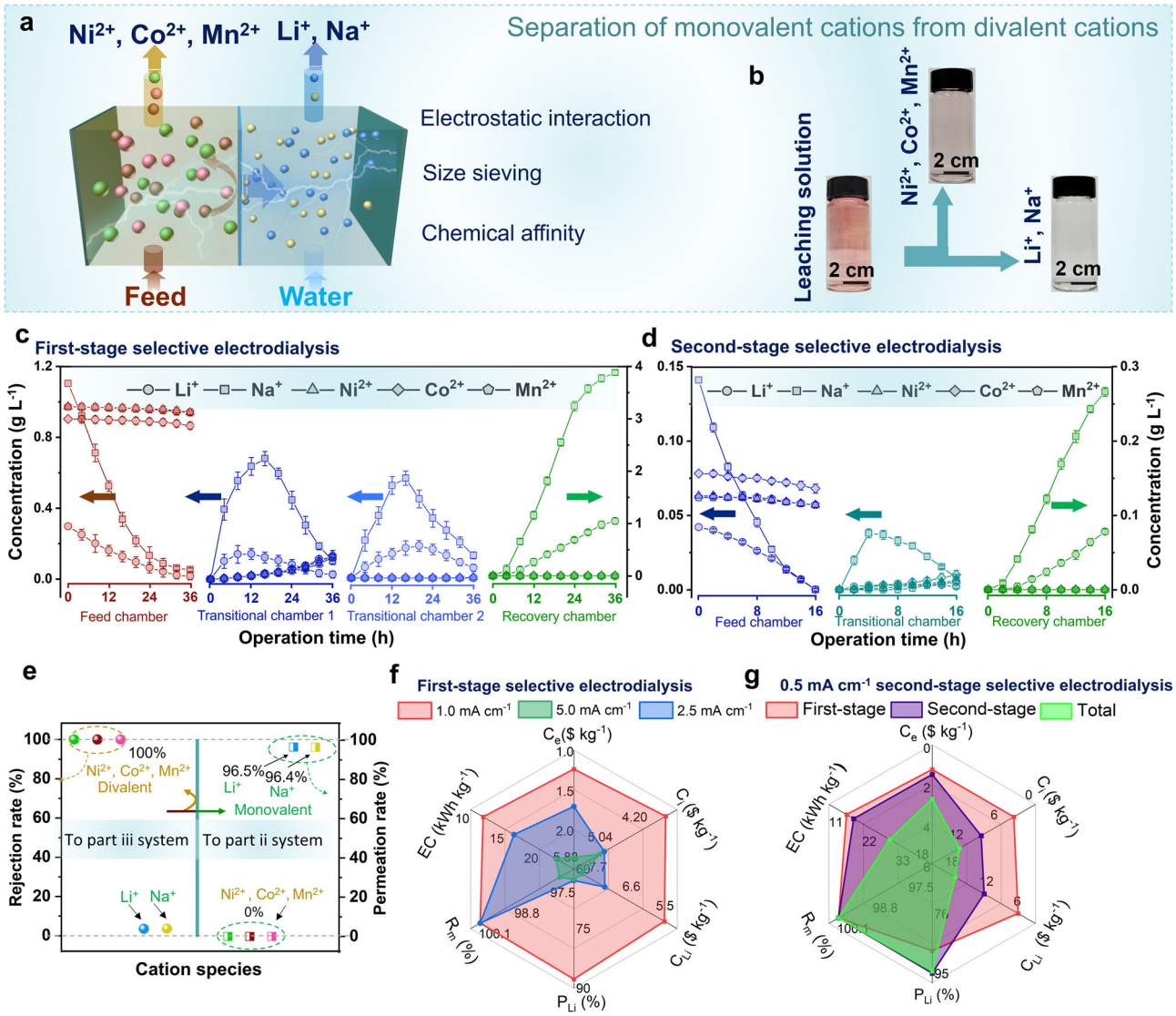

Fig. 3 | Selective separation of monovalent cations from concentrated LIB leaching solutions. a Schematic representation of the selective electrodialysis system and mechanisms governing metal ion selectivity, including size exclusion, electrostatic repulsion, and chemical affinity; **b** Color evolution of the leaching solution during separation: from dark brown (initial solution) transitions to dark red (Mn^{2+}, Ni^{2+}, and Co^{2+}-rich solution) and colorless (Li^+ and Na^+-rich solution); **c** First-stage selective electrodialysis separation of 4 L leaching solution, showing changes in metal ion concentrations (Li^+, Na^+, Mn^{2+}, Ni^{2+}, and Co^{2+}) across feed, transitional-1, transitional-2, and recovery chambers under the current density of 1.0 mA cm^{-2}; **d** Second-stage selective electrodialysis separation of 2 L transitional solution, tracking concentration changes in feed, transitional and recovery chambers; **e** Separation efficiency: the cumulative recovery rates of monovalent cations (Li^+: 96.5%, Na^+: 96.4%) and rejection rates of multivalent cations (Mn^{2+}, Ni^{2+}, and Co^{2+}: 100%); **f** The energy, economic, and environmental analysis of energy consumption, energy cost, and investment cost for Li^+ recovery; **g** Optimized selective membrane dual-stage distillation performance metrics, including recovery rate (96.5%), purity (100%), and associated energy, economic and environmental costs under current density of first stage at 1 mA cm^{-2} and second-stage at 0.5 mA cm^{-2}. R_m monovalent metal ion recovery rate. P_{Li} purity of recovered Li^+. C_i investment cost. C_{Li} Li^+ recovery cost. C_e energy cost. EC energy consumption. Error bars denote the standard deviation of the means ($n = 2$). Source data are provided as a Source data file.

percentages of 29.9% Li and 45.1% O, with less than 0.1% Na (Fig. 4d). High-resolution XPS spectra of C 1s and O 1s confirm the presence of C=O and C–O bonds in those generated crystals (Supplementary Fig. 19). X-ray diffraction (XRD) analysis further confirms that all the crystals are Li_2CO_3, demonstrating a high product purity (Fig. 4e).

The temporal evolution of Li^+ and Na^+ concentrations in the bipolar membrane in situ crystallization configuration is shown in Fig. 4f. At an optimized current density of 5 mA cm^{-2}, both Li^+ and Na^+ in the feed chamber decrease to an extremely low value. In the recovery chamber, the Li^+ initially increases and then decreases to 0.1 g L^{-1} due to the in situ crystallization of Li_2CO_3 (reaction mechanisms are detailed in Supplementary Fig. 17). This process yields Li_2CO_3 crystals with >99.9% purity (Fig. 4g). Without in situ crystallization, >99.0% of both Li^+ and Na^+ would be recovered (Fig. 4g and Supplementary Fig. 20). With this optimized configuration, >98.0% of Li^+ is recovered from the leaching solution (achieves a recovery of 95.5% for Li^+ in the whole process), and produces Li_2CO_3 with >99.9% purity. Additionally, the NaOH (>97.5% recovery, >95% purity) is recovered and reused as a basic solution in subsequent membrane metal-complexing ex situ crystallization as well as membrane metal-extracting temporal crystallization configurations (Supplementary Fig. 21). High-purity HCl is generated for spent LIB dissolution and subsequent systems for divalent cation recovery.

This bipolar membrane in situ crystallization system not only generates high-purity Li_2CO_3 but also provides significant energy, economic, and environmental benefits. The recovered Li_2CO_3, NaOH,

https://doi.org/10.1038/s41467-025-67678-5

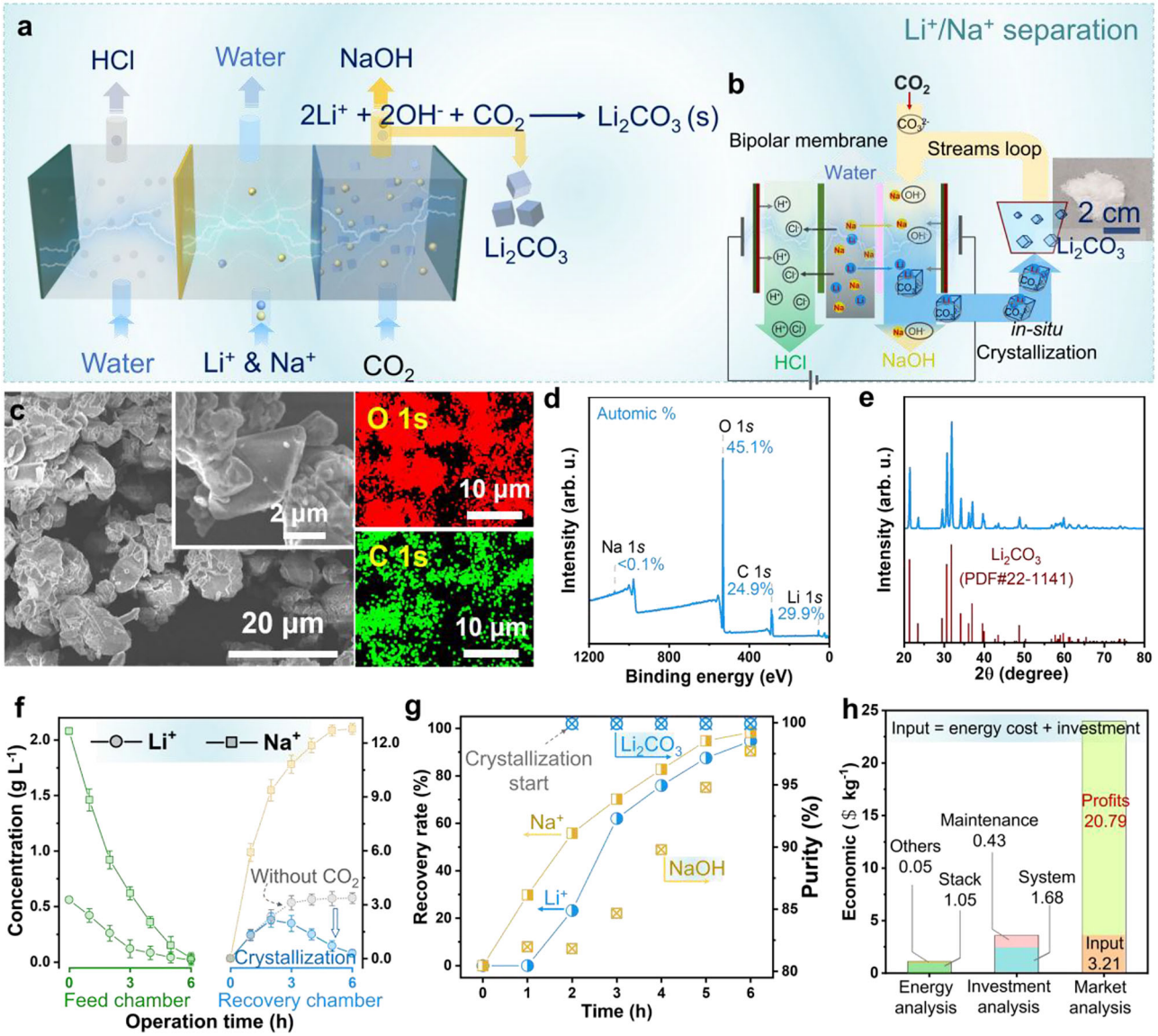

Fig. 4 | Sustainable lithium carbonate (Li_2CO_3) production from monovalent cation solution and waste CO_2. **a** Schematic of Li^+ recovery via the bipolar membrane in situ crystallization configuration and the mechanisms of Li_2CO_3 formation through utilization; **b** Operational principles of the bipolar membrane in situ crystallization system, with an inset showing the collected Li_2CO_3 powder (white); **c** SEM images of the Li_2CO_3 crystals (regular octahedral morphology, ~4 μm average diameter) and element mapping of C and O distribution; **d** XPS survey spectra of the Li_2CO_3 crystals, showing atomic percentages: Li (24.9%), O (45.1%), negligible Na (< 0.1%), and C (24.9%, with testing background); **e** XRD spectra of the synthesized crystals, confirming the crystallographic phase of Li_2CO_3. All diffraction peaks align with the standard reference pattern for lithium carbonate (PDF#22-1141), demonstrating high phase-purity and crystallinity.; **f** Temporal evolution of Li^+ and Na^+ concentrations in feed and recovery chambers under optimized current density (5 mA cm^{-2}), Li^+ depletion correlates with Li_2CO_3 crystallization, error bars denote the standard deviation of the means ($n = 2$); **g** Recovery rates (Li^+: 98.0%; Na^+: 97.5%) and product purity (Li_2CO_3: > 99.9%; NaOH: 95%); **h** The energy, economic and environmental analysis of the bipolar membrane in situ crystallization system: energy cost (1.10 $ kg^{-1} Li_2CO_3), investment (2.11 $ kg^{-1} Li_2CO_3), and profits (20.79 $ kg^{-1} Li_2CO_3) relative to market price of Li_2CO_3 (24.00 $ kg^{-1}). Source data are provided as a Source data file.

and HCl mitigate environmental pollution of discharged metal ions and safety risks associated with high metal ion concentrations while offering valuable ion resources for industrial applications. Measuring by economic efficiency of per $ kg^{-1} Li_2CO_3, as shown in Fig. 4h, the economic analysis reveals that the primary costs are energy consumption (1.10 $ kg^{-1} Li_2CO_3) and investment (membranes: 1.68 $ kg^{-1} Li_2CO_3, maintenance: 0.43 $ kg^{-1} Li_2CO_3). Given the current market price of Li_2CO_3 (24.00 $ kg^{-1}), the system yields a profit of around 20.79 $ kg^{-1} Li_2CO_3 (Supplementary Tables 10 and 11). Beyond the Li_2CO_3 profits, this configuration also generates NaOH and HCl for supporting other LIB recycling configurations, along with environmental benefits such as CO_2 fixation and zero liquid discharge. Despite those advantages, the system faces limitations of the current electro-driven membranes due to the low ion throughput and poor anti-scaling properties (Supplementary Fig. 22 and Fig. 23). Future work should focus on improving electro-membrane performance to enhance the metal ion throughput and mitigate electro-membrane issues that enable more efficient and sustainable LIB recycling.

Recovery of Mn^{2+}, Ni^{2+}, and Co^{2+}

The tandem leaching streams from the selective membrane dual-stage distillation system contain Mn^{2+}, Ni^{2+}, and Co^{2+}, which are extracted as valuable metals from the black mass obtained after precise dismantling and separation of spent LIBs. To recover those metal ions, the membrane metal-complexing ex situ crystallization, as well as membrane metal-extracting temporal crystallization configurations, are

https://doi.org/10.1038/s41467-025-67678-5

developed, as illustrated in Fig. 5a. These systems exploit differential coordination behavior of Mn^{2+}, Ni^{2+}, and Co^{2+} to ethylenediaminetetraacetic acid (EDTA) and the extractant Cyanex 272 to selectively recover Mn_3O_4, $Ni(OH)_2$, and $Co(OH)_2$, respectively (Fig. 5b). According to coordination capacity to the EDTA complexing agent, in the membrane metal-complexing ex situ crystallization configuration, Ni^{2+} and Co^{2+} exhibits significantly higher coordination capacity with EDTA than Mn^{2+}, thus forming $[EDTA\text{-}Ni]^{2-}$ ($K_{Ni} = 2.51 \times 10^{18}$) and $[EDTA\text{-}Co]^{2-}$ ($K_{Co} = 2.82 \times 10^{16}$) (Supplementary Figs. 24 and 25). In contrast, Mn^{2+} exhibits a significantly lower coordination capacity with EDTA ($K_{Mn} = 7.76 \times 10^{13}$). Consequently, Mn^{2+} migrates to the recovery chamber, where it chemically reacts with the extra-added OH^- (supplied from the bipolar membrane in situ crystallization system) to precipitate as $Mn(OH)_2$, which then is oxidized to Mn_3O_4 under ambient conditions (25 °C) (Fig. 5ci). Following, the complexing anions of $[EDTA\text{-}Ni]^{2-}$ and $[EDTA\text{-}Co]^{2-}$ are retained in the collecting chamber of the membrane metal-complexing ex situ crystallization system. The influence of the EDTA: (Ni+Co) molar ratio, including 0.95, 1.0, 1.05, and 1.15, on metal ion separation is explored (Supplementary Fig. 26). The concentrations of Ni^{2+}, Co^{2+}, and Mn^{2+} in the feed chamber present a decreasing trend (Figs. S26a–c). The Ni^{2+} and Co^{2+} form $Ni[EDTA]^{2+}$/$Co[EDTA]^{2+}$ complex anions, thus they migrate toward the

Fig. 5 | Recycling of Mn^{2+}, Ni^{2+}, and Co^{2+} from the divalent cation solutions. **a** Schematic of the subsequent membrane metal-complexing ex situ crystallization as well as membrane metal-extracting temporal crystallization configurations for sequential separation of Mn^{2+}, Ni^{2+}, and Co^{2+}; **b** Mechanisms of the EDTA complexion (selective coordination with Ni^{2+} and Co^{2+}) and the Cyanex 272 extraction (preferential binding to Co^{2+}), enabling targeted metal recovery; **c** Photographs of recovered products, (i) black Mn_3O_4, (ii) green $Ni(OH)_2$, and (iii) pink $Co(OH)_2$ powders; **d** SEM images and elemental mapping of Mn_3O_4, $Ni(OH)_2$ and $Co(OH)_2$ crystals, respectively, confirming uniform morphology and homogeneous distribution of Mn, Ni, and Co; **e** XPS spectra showing atomic compositions of (i) Mn_3O_4 (Mn: 26.9%, O: 37.6%), (ii) $Ni(OH)_2$ (Ni: 29.1%, O: 56.3%), and (iii) $Co(OH)_2$ (Co: 23.7%, O: 54.9%), with < 0.1% impurities; **f** XRD spectra confirming phase-pure Mn_3O_4 (PDF#24-0734), $Ni(OH)_2$ (PDF#14-0117), and $Co(OH)_2$ (PDF#30-0443) powders, with no impurity peaks; **g** Temporal evolution of Mn^{2+}, Ni^{2+}, and Co^{2+} concentrations in membrane metal-complexing ex situ crystallization system, achieving > 99.5% Mn^{2+} at 5 mA cm^{-2} and at EDTA: (Ni + Co) of 1.05; **h** Temporal evolution of Ni^{2+} and Co^{2+} concentrations in membrane metal-extracting temporal crystallization system, recovering > 83.1% Ni^{2+} and > 87.3% Co^{2+}; **i** Recovery and product purity of Mn_3O_4 (> 99.5% recovery, > 9.9% purity), $Ni(OH)_2$ (> 83.1% recovery, > 99.5% purity), and $Co(OH)_2$ (> 87.3% recovery, > 92.5% purity). **j** The energy, economic, and environmental analysis: energy consumption (Mn_3O_4: 1.30 \$ kg^{-1} Mn_3O_4; $Ni(OH)_2$ and $Co(OH)_2$: 1.89 \$ kg^{-1} [$Ni(OH)_2$ + $Co(OH)_2$]), investment costs (Mn_3O_4: 1.02 \$ kg^{-1} Mn_3O_4; $Ni(OH)_2$ and $Co(OH)_2$: 1.86 \$ kg^{-1} [$Ni(OH)_2$ + $Co(OH)_2$]), and net profits (Mn_3O_4: 6.68 \$ kg^{-1} Mn_3O_4; $Ni(OH)_2$ and $Co(OH)_2$: 12.37 \$ kg^{-1} [$Ni(OH)_2$ + $Co(OH)_2$]). Error bars denote the standard deviation of the means ($n = 2$). Source data are provided as a Source data file.

anode into the chamber. On the contrary, the Mn^{2+} migrates toward the cathode into the recovery chamber as the experiment progresses (Supplementary Fig. 26f). A small amount of Ni^{2+} and Co^{2+} is also recovered along with Ni^{2+} when the molar ratio of EDTA to Ni+Co at 1, due to the incomplete complexation (Supplementary Figs. 26d, e). As the molar ratio of EDTA to Ni+Co increases to 1.05, no extra Ni^{2+} and Co^{2+} ions are observed in the recovery chamber, and Mn^{2+} approaches the highest recovery. However, a further increase in the molar ratio to 1.15 significantly decreases the recovery efficiency of Mn^{2+} due to the formation of $Mn[EDTA]^{2+}$. Considering the higher recovery of Mn^{2+}, the molar ratio of EDTA to Ni+Co is optimized at 1.05. With the extra-added H^+, which is supplied from the bipolar membrane in situ crystallization, $[EDTA\text{-}Ni]^{2-}$ and $[EDTA\text{-}Co]^{2-}$ de-coordinate with EDTA, and the subsequent separation is carried out in the membrane metal-extracting temporal crystallization configuration. Based on the higher affinity capacity to Cyanex 272, the Co^{2+} is more likely to form complex Co(Cyanex 272)$_2$ and remain in the solution (Supplementary Figs. 27 and 28). Meanwhile, the Ni^{2+} migrates to the recovery chamber under the electrical field and is finally recovered as the green crystal of $Ni(OH)_2$ (Fig. 5cii). With temporal control, the pink $Co(OH)_2$ is finally obtained from the extracted chamber of the membrane metal-extracting temporal crystallization system (Fig. 5ciii).

SEM imaging reveals distinct crystal morphologies with uniform elemental distribution for Mn, Ni, and Co, respectively (Fig. 5d). Various specific crystal structures with different diameters and high homogeneity of the elements' distribution can be observed from those images. The XPS spectra results confirm high purity (> 99.5%) of all obtained metal ion products (Fig. 5e), with high-resolution spectra validating bonding environments of Mn, Ni, and Co, respectively (Supplementary Figs. 29-31). The XRD analysis confirms phase-purity of the Mn_2O_3, $Ni(OH)_2$, and $Co(OH)_2$, respectively, with no other impurity peaks in each of the XRD spectra (Fig. 5f). The temporal evolution of Ni^{2+}, Co^{2+}. and Mn^{2+} concentrations in each chamber are measured using inductively coupled plasma optical emission spectrometry (ICP-OES). In the membrane metal-complexing ex situ crystallization configuration (Fig. 5g), the Ni^{2+} and Co^{2+} form $[EDTA\text{-}Ni]^{2-}$ and $[EDTA\text{-}Co]^{2-}$ and migrate to the Ni & Co collect chamber in the anode side, while Mn^{2+}, which remains uncomplexed, transports toward the cathode into the Mn recovery chamber. Then $[EDTA\text{-}Ni]^{2-}$ and $[EDTA\text{-}Co]^{2-}$ are decomplexed using 2.0 M H_2SO_4, the collected Ni and Co solution is used in the next membrane metal-extracting temporal crystallization configuration (Fig. 5h). In the first 10 h, the Co^{2+} accumulates in the co-extraction chamber as the Co^{2+} complexes with Cyanex 272, forming non-charged Co(Cyanex 272)$_2$, while positively charged Ni^{2+} migrates to the recovery chamber. After 10 h, Co(Cyanex 272)$_2$ is dissociated into Co^{2+}, which is transported to the recovery chamber later.

In the membrane metal-complexing ex situ crystallization system, with the optimized current density of 5 mA cm^{-2}, the results reveal more than 99.5% Mn^{2+} recovery, and yield Mn_3O_4 with purity higher than 99.9% (Fig. 5i). Residual $[EDTA\text{-}Ni]^{2-}$ and $[EDTA\text{-}Co]^{2-}$ are retained in the collection chamber, ensuring freshwater reclamation and zero waste discharge. In the membrane metal-extracting temporal crystallization configuration, with optimized operating conditions, Ni^{2+} and Co^{2+} are recovered with recoveries of higher than 83.1% and 87.3%, generating the final products of $Ni(OH)_2$ and $Co(OH)_2$ with more than 99.5% and 92.5% purity, respectively (Fig. 5i).

The recovery of high-purity Mn_3O_4, $Ni(OH)_2$, and $Co(OH)_2$ not only addresses the heavy metal ion pollution but also delivers significant economic benefits. Taking Mn_3O_4 as an example, in the membrane metal-complexing ex situ crystallization configuration, taking the economic efficiency per \$ kg^{-1} Mn_3O_4, the energy consumption and investment costs are 1.30 and 1.02 \$ kg^{-1} Mn_3O_4, respectively (Fig. 5j). With a market price of ~9.00 \$ kg^{-1} Mn_3O_4, this configuration yields profits of 6.68 \$ kg^{-1} Mn_3O_4 (Supplementary Table 12). In the membrane metal-extracting temporal crystallization configuration, measured by economic efficiency of per \$ kg^{-1} [$Ni(OH)_2$ + $Co(OH)_2$] (with the mole ratio of 47:53), the energy consumption and investment costs are 1.89 and 1.86 \$ kg^{-1} [$Ni(OH)_2$ + $Co(OH)_2$], respectively (Fig. 5j). Given market prices of > 14 \$ kg^{-1} for $Ni(OH)_2$ and > 18 \$ kg^{-1} for $Co(OH)_2$, this system brings a profit at least 12.37 \$ kg^{-1} [$Ni(OH)_2$ + $Co(OH)_2$] (Supplementary Table 13). Compared to the mainstream technologies for Li recovery, the e-MCGR technology not only achieves a lower overall cost but also offers distinct profit advantages (Supplementary Table 14). Besides these energy consumptions, the extra NaOH and HCl are supplied and reused from the bipolar membrane in situ crystallization system. The EDTA and the Cyanex 272 are recycled in membrane metal-complexing ex situ crystallization and membrane metal-extracting temporal crystallization systems, which minimize reagent consumption and enhance the system's circularity. Considering the recovery rate of those metal ions, the profits could be improved when using the electro-driven membrane with high metal ion transport capacity in this configuration. Despite its energy, economic, and environmental advantages, those systems face challenges, particularly mineral scaling on electro-membranes, which limits metal ion throughput and recovery efficiency (Supplementary Fig. 32). To address these limitations, future efforts should focus on designing electro-membranes with higher ion transport capacity and enhanced anti-scaling properties. A fundamental study in advancing the understanding of metal ion crystallization kinetics in electro-membrane systems is essential to optimize recovery processes.

Recovery of metal ions from real LIBs leachate

The e-MCGR process for efficient LIBs recycling is further validated using real leachate from spent NMC111 cathode material (Fig. 6a). In the first-stage selective electrodialysis, operated at a current density of 1.0 mA cm^{-2}, the CIMS membranes effectively reject multivalent metal ions (Mn^{2+}, Ni^{2+}, and Co^{2+}) and permeate monovalent metal ions (Na^+ and Li^+). Thus, the concentrations of Li^+ and Na^+ increase to 1.08 g L^{-1} and 3.73 g L^{-1} in the recovery chamber, respectively (Fig. 6b). The residual solutions from the transitional chambers (in both transitional

https://doi.org/10.1038/s41467-025-67678-5

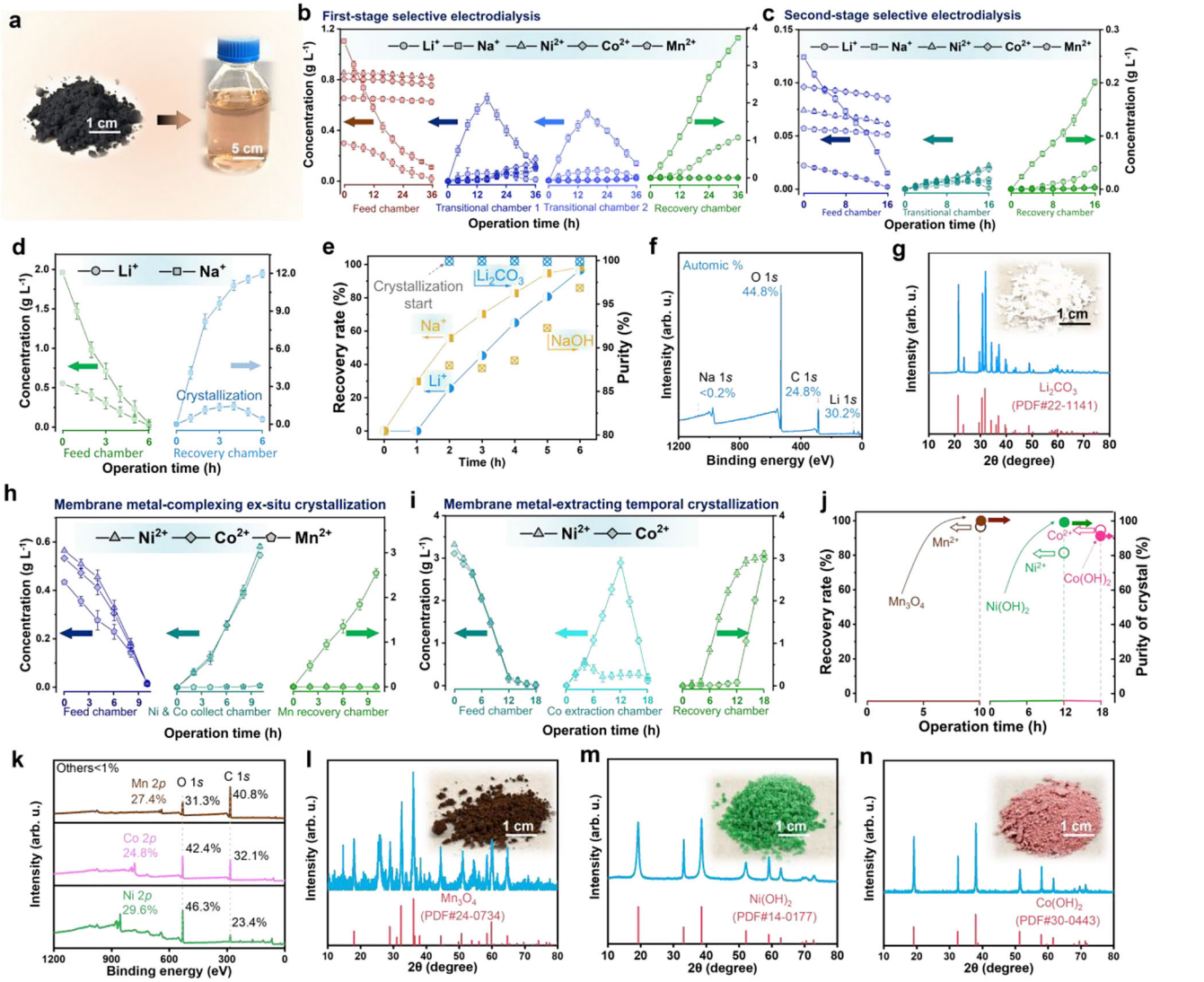

Fig. 6 | Recovery of lithium and metal salts from real LIBs leaching solutions. **a** Photo of spent LIBs leachate; **b** First-stage selective electrodialysis separation of monovalent cations (Li^+ and Na^+) from divalent cations (Mn^{2+}, Ni^{2+}, and Co^{2+}) under the current density of 1.0 mA cm^{-2}; **c** Second-stage selective electrodialysis separation of transitional solution for enhanced monovalent selectivity; **d** Temporal evolution of Li^+ and Na^+ concentrations under current density of 5 mA cm^{-2} in bipolar membrane in situ crystallization process; **e** Recovery rates and product purity; **f** XPS spectra showing atomic compositions of Li_2CO_3 crystals (Li: 30.2%, O: 44.8%, C: 24.8%); **g** XRD spectra of the synthesized crystals; **h** Temporal evolution of Mn^{2+}, Ni^{2+}, and Co^{2+} concentrations in membrane metal-complexing ex situ crystallization system; **i** Temporal evolution of Ni^{2+} and Co^{2+} concentrations in membrane metal-extracting temporal crystallization system; **j** Recovery and product purity of Mn_3O_4 (> 94.5% recovery, > 99.8% purity), $Ni(OH)_2$ (> 80.1% recovery, > 99.3% purity), and $Co(OH)_2$ (> 95.6% recovery, > 92.2% purity); **k** XPS spectra showing atomic compositions of (i) Mn_3O_4 (Mn: 27.4%, O: 31.3%), with < 0.3% impurities, (ii) $Ni(OH)_2$ (Ni: 29.6%, O: 46.3%), and (iii) $Co(OH)_2$ (Co: 24.8%, O: 42.4%), with < 1.0% impurities; **l** XRD spectra confirming phase-pure Mn_3O_4 (PDF#24-0734) powder; **m** XRD spectra confirming phase-pure $Ni(OH)_2$ (PDF#14-0117) powder; **n** XRD spectra confirming phase-pure $Co(OH)_2$ (PDF#30-0443) powder. Error bars denote the standard deviation of the means ($n = 2$). Source data are provided as a Source data file.

chamber-1 and transitional chamber-2) in the first-stage selective electrodialysis are then fed into the second-stage selective electrodialysis for further separation (Fig. 6c). This selective membrane dual-stage distillation configuration achieves accumulative recovery of 93.9% for Li^+ and 89.1% for Na^+, while completely rejecting Mn^{2+}, Ni^{2+} and Co^{2+}. This process demonstrates a low energy cost (1.56 \$ kg^{-1}), investment cost (7.08 \$ kg^{-1}), and energy consumption (14.87 kWh kg^{-1}) (Supplementary Table 15).

Subsequent bipolar membrane in situ crystallization process recovers 96.6% Li^+ from the leaching solution and produces Li_2CO_3 with > 99.9% purity (Fig. 6d, e). XPS analysis confirm the product's composition, showing atomic percentages of 32.2% Li, and 39.6% O, with others less than 0.3% (Fig. 6f). The high purity of 99.9% was further verified by XRD analysis (Fig. 6g). The economic analysis reveals that the primary costs are energy consumption (0.72 \$ kg^{-1} Li_2CO_3) and investment cost (2.12 \$ kg^{-1} Li_2CO_3). Given the current market price of Li_2CO_3 (24.00 \$ kg^{-1}), the system yields a profit of around 21.16 \$ kg^{-1} Li_2CO_3 (Supplementary Table 16). Moreover, 97.7% NaOH with 96.7% purity is recovered from the bipolar membrane in situ crystallization process.

In membrane metal-complexing ex situ crystallization, due to its lower coordination capacity with EDTA, Mn^{2+} migrates to the recovery chamber (Fig. 6h). In a separate membrane metal-extracting temporal crystallization step, Ni^{2+} migrates to the recovery chamber and is recovered as $Ni(OH)_2$ by adding NaOH (Fig. 6i). With temporal control, the pink $Co(OH)_2$ is subsequently obtained from the extraction chamber. The membrane metal-complexing ex situ crystallization proves optimal for maximizing the recovery rate and product purity for all transition metals (Fig. 6j). The XPS spectra results confirm high purity (> 92.0%) of all obtained metal ion products (Fig. 6k). The XRD

analysis confirms the generation of Mn_3O_4 (Fig. 6l). The energy consumption and investment costs are 1.42 and 1.46 $ kg^{-1} Mn_3O_4, respectively. With a market price of ~9.00 $ kg^{-1} Mn_3O_4, this configuration yields profits of 6.12 $ kg^{-1} Mn_3O_4 (Supplementary Table 17). XRD analysis confirmed the phase-purity of the recovered $Ni(OH)_2$ and $Co(OH)_2$ (Fig. 6m, n). The process achieved an 80.1% recovery of $Ni(OH)_2$ with 99.3% purity and, with temporal control, a 95.6% recovery of pink $Co(OH)_2$ with 92.2% purity. The combined energy consumption and investment costs for recovering $Ni(OH)_2$ + $Co(OH)_2$ are 1.61 and 1.93 $ kg^{-1} [$Ni(OH)_2$ + $Co(OH)_2$], respectively. Given market prices of > 14 $ kg^{-1} for $Ni(OH)_2$ and > 18 $ kg^{-1} for $Co(OH)_2$, this system brings a profit of 12.58 $ kg^{-1} [$Ni(OH)_2$ + $Co(OH)_2$] (Supplementary Table 18).

Discussion

This work presents a highly modular platform for recycling spent lithium-ion batteries (LIBs) through an electro-membrane crystallization-assisted general recycling (e-MCGR) concept and technology. This e-MCGR incorporates four key configurations: (1) selective membrane dual-stage distillation for Li^+ and Na^+ separation from multivalent cations (Mn^{2+}, Ni^{2+}, and Co^{2+}), (2) bipolar membrane in situ crystallization for Li_2CO_3 recovery and CO_2 utilization, (3) membrane metal-complexing ex situ crystallization for Mn_3O_4 recovery, and (4) membrane metal-extracting temporal crystallization for $Ni(OH)_2$ and $Co(OH)_2$ recovery. These configurations enable the efficient separation and recovery of valuable metal ions, including Li^+, Mn^{2+}, Ni^{2+}, and Co^{2+}, from LIB leaching solutions, achieving high recoveries and crystal product purity. The proposed system not only addresses resource scarcity and environmental pollution but also delivers significant economic benefits. The recovery of high-purity Li_2CO_3, Mn_3O_4, $Ni(OH)_2$, and $Co(OH)_2$ generates substantial profits, and the reuse of NaOH, HCl, and recycling of EDTA/Cyanex 272 minimizes waste and enhances sustainability. The novel design concepts, technological principles, and evaluation methods demonstrated in this work pave the way for the development of high-efficiency and economically viable LIB recycling systems. This e-MCGR technology can be integrated with intermittent energy systems and sustainable resource management. To further advance this technology, future efforts should focus on developing advanced electro-driven membranes with high metal ion permeation rates, enhanced target ion selectivity, and superior anti-scaling properties.

Methods

Pretreatment

The suspended solids in the feed are removed by using ultrafiltration (UP150 membrane) at an operating pressure of 0.01 MPa. Then the permeate is concentrated using reverse osmosis (RO, BW30 membrane) at an operating pressure of 1.5 MPa.

Configurations in the e-MCGR process

All experimental configurations described herein are conducted using a single, consistently prepared complex feed batch (the composition is shown in Supplementary Table 7) to ensure comparability and integration across the e-MCGR process. This batch simulated real LIB leachate is used sequentially across all experimental stages without intermediate reconstitution (Supplementary Table 19). The integrated design of the e-MCGR process comprises:

i. Selective membrane dual-stage distillation configuration: This configuration employs two sequential selective electro-membrane stacks to separate monovalent metal ions (Li^+ and Na^+) from the divalent metal ions (Mn^{2+}, Ni^{2+}, and Co^{2+}). In the first-stage selective electro-membrane stack (Supplementary Fig. 6), the membranes are arranged as: anode / bipolar membrane (BM) / AMX (commercial anion exchange membrane) × 3 / CIMS (commercially monovalent cation exchange membrane) × 3 / bipolar membrane (BM) / cathode (Supplementary Table 20). The effective area per membrane is 0.0189 m^2. Four chambers (feed, transitional-1, transitional-2, recovery) are connected to containers holding 2 L simulated LIB leaching solution in the feed chamber and 0.5 L deionized water in the other chambers. The operational parameters of the current densities are tested at 1 mA cm^{-2}, 2.5 mA cm^{-2}, and 5 mA cm^{-2}. The electric current of the electro-membrane stack is supplied by a stabilized power supply. In order to further distill Li^+ and Na^+ from transitional chambers (transitional chamber-1 and transitional chamber-2) of the first stage, the second-stage selective electro-membrane stack is developed (Supplementary Fig. 6), and the electro-membrane stack arrangement is anode / BM / AMX × 2 / CIMS × 2 / BM/cathode. Three chambers in the electro-membrane stack consist of the feed chamber, the transitional chamber, and the recovery chamber. For those chambers, 1 L of residual solution from the first-stage transitional chambers is introduced into the feed chamber of the second-stage stacks, and the transitional and recovery chambers are initially fed with 0.5 L of deionized water. The current density of the electro-membrane stack is 0.5 mA cm^{-2}. The refined Li^+ and Na^+ from the recovery chamber are then directly used as feed for the subsequent bipolar membrane in situ crystallization (ii) to separate Li^+ from Na^+.

ii. Bipolar membrane in situ crystallization configuration: In this configuration, the electro-membranes are stacked between anode and cathode in a sequence of the anode / BM / AMX / commercial cation exchange membrane (CMX) / BM / cathode (Supplementary Fig. 13), forming three chambers, including the feed chamber, the acid chamber, and the base chamber. Specifically, 1 L monovalent metal ions solution (Li^+ and Na^+) from the recovery chambers of configuration (i) is used as the initial feed, and 0.5 L of deionized water is fed to the acid and base chambers. The electric current of this electro-membrane stack is 5 mA cm^{-2}, which is supplied by a direct current-stabilized power supply. To avoid Na^+ impurities in Li_2CO_3 (caused by Na_2CO_3 co-precipitation) and capture the CO_2 from industry, CO_2 gas is introduced into the base chamber as a carbonate source, at a constant flow rate of 50 mL min^{-1} (Supplementary Fig. 14). During the reaction, CO_2 dissolves into the solution and subsequently forms carbonate species. The Li_2CO_3 crystals will be crystallized in the base solution, followed by Li_2CO_3 recovery with the UP150 membrane.

$$CO_2 + 2OH^- \rightarrow CO_3^{2-} + H_2O$$

Then, Li_2CO_3 crystallization occurs as

$$CO_3^{2-} + 2Li^+ \rightarrow Li_2CO_3 (K_{sp} = 8.15 \times 10^{-4})$$

Overall, the reaction is

$$2OH^- + CO_2 + 2Li^+ \rightarrow Li_2CO_3 \downarrow + H_2O$$

iii. Membrane metal-complexing ex situ crystallization configuration: Here, the membrane sequence is: anode / CMX / AMX / CMX / AMX / cathode (Supplementary Fig. 19), with three chambers: the feed, complexing, and the recovery chamber. The residual divalent metal-rich solution remaining after configuration (i) serves as the feed for this configuration. Herein, 3.0 L mixtures of Mn^{2+}, Ni^{2+}, and Co^{2+} are introduced into the feed chamber, and 0.5 L of deionized water is fed into the complexing and recovery chambers. The feed solution is further treated with the EDTA-4Na salt in the feed container. When the $[EDTA]^{4-}$ forms complex anions with Ni^{2+} and Co^{2+}, with the EDTA's differential coordination capacities ($K_{Ni} > K_{Co} \gg K_{Mn}$), the Mn^{2+} is separated from Ni^{2+} and Co^{2+} using this membrane metal-complexing ex situ crystallization system,

$$Ni^{2+} + EDTA^{4-} \rightarrow [EDTA - Ni]^{2-} \quad K_{Ni} = 2.51 \times 10^{18}$$

$$Co^{2+} + EDTA^{4-} \rightarrow [EDTA - Co]^{2-}\ K_{Co} = 2.82 \times 10^{16}$$

$$Mn^{2+} + EDTA^{4-} \rightarrow [EDTA - Mn]^{2-}\ K_{Mn} = 7.76 \times 10^{13}$$

For the decomplexation, EDTA complexes are dissociated by adding 2.0 M HCl until pH < 0.5. To recover metal ions, Mn^{2+} in the recovery chamber is precipitated as $Mn(OH)_2$ by using 1.0 M NaOH. Both the acid and base used here are provided by configuration (ii).

$$Mn^{2+} + 2OH^- \rightarrow Mn(OH)_2 \downarrow$$

Then, the $Mn(OH)_2$ is oxidized to black Mn_3O_4 crystals

$$6Mn(OH)_2 + O_2 \rightarrow 2Mn_3O_4 \downarrow + 6H_2O$$

Membrane metal-extracting temporal crystallization configuration: Connecting with the membrane metal-complexing ex situ crystallization configuration, this stack uses: anode / AMX / CMX / CMX / AMX / cathode (Supplementary Fig. 19). In this system, the membrane stack contains three containers, which connect with the feed chamber, the Co-extraction chamber, and the Ni-recovery chamber. The containers are initially fed with 0.5 L mixed Ni^{2+} and Co^{2+} solution from the membrane metal-complexing ex situ crystallization system, 0.5 L extraction solution (50% saponified Cyanex 272 in kerosene), and 0.5 L deionized water, respectively. The electric current of the complexation electrodialysis stack is tested at 5 mA cm^{-2}. Due to the Cyanex 272 preferentially binds Co^{2+}, it enables efficient Ni^{2+} and Co^{2+} separation. In this process, the Co^{2+} is extracted by Cyanex 272, which forms a stable complex with Cyanex 272 in the extraction chamber.

$$Co^{2+} + 2\ \text{Cyanex 272} \rightarrow Co\ (\text{Cyanex272})_2 + 2H^+$$

Then, the uncomplexed Ni^{2+} migrates to the Ni-recovery chamber under the electric field. The Ni^{2+} is precipitated as $Ni(OH)_2$ with the usage of 1.0 M NaOH (supplied from the bipolar membrane in situ crystallization system).

$$Ni^{2+} + 2OH^- \rightarrow Ni(OH)_2 \downarrow$$

With temporal crystallization of Ni^{2+}, 2.0 M HCl is added to the feed chamber to release CO^{2+} from Cyanex 272,

$$Co(\text{Cyanex272})_2 + 2H^+ \rightarrow Co^{2+} + 2\ \text{Cyanex 272}$$

Then, these Co^{2+} migrate to the Co-recovery chamber under the electric field and precipitate as $Co(OH)_2$ with the usage of 1.0 M NaOH.

$$Co^{2+} + 2OH^- \rightarrow Co(OH)_2 \downarrow$$

Validation of the e-MCGR process using real LIBs wastewater

To validate the practical feasibility of the e-MCGR process, real wastewater from spent ternary LIBs is used as feed. The spent ternary LIBs, sourced from a technology company's power bank, are used as the primary raw materials. First, 0.4 g of waste NMC111 cathode material is leached in 4.0 M HCl at 80 °C for 6 h. The resulting leachate is subjected to the same pretreatment sequence as described in the "Pretreatment" section, namely ultrafiltration (UP150 membrane, 0.01 MPa) to remove organic impurities, followed by RO (BW30 membrane, 1.5 MPa) to concentrate the solution. The concentrated leachate, now enriched in Li^+, Na^+, Mn^{2+}, Ni^{2+}, and Co^{2+}, is directly used as the feed for the e-MCGR process, without reconstitution or modification, to ensure a one-to-one comparison with the results obtained from the simulated LIB leachate.

Characterization methods

The chemical composition and bonding states of the recovered crystals are analyzed by using X-ray photoelectron spectroscopy (XPS; AXIS UltraDLD, Shimadzu, Japan). Scanning electron microscopy (SEM; Sirion 200, FEI, USA) coupled with energy-dispersive spectroscopy (EDS; INCA X-Act, USA) is employed to assess crystal morphology, surface roughness, and elemental distribution. The crystal phase identification is performed through X-ray diffractometry (XRD; XRD-6100, Shimadzu, Japan) using Cu-Kα radiation (λ = 1.5 Å). Metal ion concentrations are quantified by using Inductively Coupled Plasma Optical Emission spectroscopy (ICP-OES; Avio 500, PerkinElmer, USA). The properties of ion exchange membranes used in the study are shown in Supplementary Table 12.

Evaluation methods

Technological analysis. Metal ion selectivity (P) is a parameter that is used to illustrate membrane ion selectivity. Compared to other metal ions (M^{z+}), the target metal ion selectivity can be calculated as

$$P = \frac{T_{target}/T_m}{c_{target}/c_m} = \frac{J_{target} \cdot c_m}{J_m \cdot c_{target}} \quad (1)$$

Where T_{target} and T_m are the transport numbers of target metal ions and other metal ions. c (mol L^{-1}) is the concentration of metal ions. J (mol m^{-2} s^{-1}) is the metal ion permeation rate, which is used to illustrate ion transport capacity, and can be calculated as

$$J = \frac{V\frac{dc}{dt}}{S} \quad (2)$$

Where V (L) is the volume of solution, and S (m^2) is the membrane area.

The product recovery rate (R, %) is calculated by,

$$R = \frac{m_t}{m} \quad (3)$$

where m_t (g) is the mass of precipitate recovered at time t, and m (g) is the theoretical maximum precipitate mass.

The equation of total suspended solids measurement, which is the crystal yield (Y, g L^{-1}),

$$Y = \frac{m_{cry}}{V_{brine}} \quad (4)$$

where m_{cry} is the mass of dried crystals, and V_{brine} (L) is the volume of feed wastewater.

Energy, economic, and environmental analysis. In this e-MCGR process, the specific energy consumption (E, kWh kg^{-1}) is calculated by,

$$E = \int_0^t \frac{U_t I d_t}{C_t V_t M} \quad (5)$$

where U_t (V) is the electro-membrane stack voltage, I (A) is the current, V_t (L) is the volume of solution, C_t (mol L^{-1}) is the concentration, and M (g mol^{-1}) is the molecular mass. More data on energy, economics, and the environment on this e-MCGR technology are analyzed and summarized in the Supplementary Information.

Data availability

The data generated in this study are provided in the article and its Supplementary Information. Visualization and figure preparation are carried out using Origin 8, Microsoft PowerPoint 2021, and Microsoft Excel 2021. Source data are provided with this paper.

References

1. Pomerantseva, E. et al. Energy storage: the future enabled by nanomaterials. *Science* **366**, eaan8285 (2019).
2. Tao, Y. et al. Second life and recycling: energy and environmental sustainability perspectives for high-performance lithium-ion batteries. *Sci. Adv.* **7**, eabi7633 (2021).
3. Harper, G. et al. Recycling lithium-ion batteries from electric vehicles. *Nature* **575**, 75–86 (2019).
4. Niu, B. et al. Recycling hazardous and valuable electrolyte in spent lithium-ion batteries: urgency, progress, challenge, and viable approach. *Chem. Rev.* **123**, 8718–8735 (2023).
5. Ma, R. et al. Pathway decisions for reuse and recycling of retired lithium-ion batteries considering economic and environmental functions. *Nat. Commun.* **15**, 7641 (2024).
6. Ji, G. et al. Direct regeneration of degraded lithium-ion battery cathodes with a multifunctional organic lithium salt. *Nat. Commun.* **14**, 584 (2023).
7. Baars, J. et al. Circular economy strategies for electric vehicle batteries reduce reliance on raw materials. *Nat. Sustain.* **4**, 71–79 (2020).
8. Yang, T. et al. Sustainable regeneration of spent cathodes for lithium-ion and post-lithium-ion batteries. *Nature Sustain* **7**, 776–785 (2024).
9. Kim, K. et al. Selective cobalt and nickel electrodeposition for lithium-ion battery recycling through integrated electrolyte and interface control. *Nat. Commun.* **12**, 6554 (2021).
10. Zhao, Y. et al. Recycling of sodium-ion batteries. *Nat. Rev. Mater.* **8**, 623–634 (2023).
11. Kazi, O. A. et al. Material design strategies for recovery of critical resources from water. *Adv. Mater.* **35**, e2300913 (2023).
12. Ji, G. et al. Sustainable upcycling of mixed spent cathodes to a high-voltage polyanionic cathode material. *Nat. Commun.* **15**, 4086 (2024).
13. Zhao, Y. et al. Advanced ion transfer materials in electro-driven membrane processes for sustainable ion-resource extraction and recovery. *Prog. Mater. Sci.* **128**, 100958 (2022).
14. Xu, X. et al. Extraction of lithium with functionalized lithium ion-sieves. *Prog. Mater. Sci.* **84**, 276–313 (2016).
15. Srimuk, P. et al. Charge-transfer materials for electrochemical water desalination, ion separation and the recovery of elements. *Nat. Rev. Mater.* **5**, 517–538 (2020).
16. Lei, S., Sun, W. & Yang, Y. Solvent extraction for recycling of spent lithium-ion batteries. *J. Hazard. Mater.* **424**, 127654 (2022).
17. Krishnan, S. et al. Current technologies for recovery of metals from industrial wastes: an overview. *Environ. Technol. Innov.* **22**, 101525 (2021).
18. Mossali, E. et al. Lithium-ion batteries towards circular economy: a literature review of opportunities and issues of recycling treatments. *J. Environ. Manage.* **264**, 110500 (2020).
19. Wang, M. et al. Selective extraction of critical metals from spent lithium-ion batteries. *Environ. Sci. Technol.* **57**, 3940–3950 (2023).
20. Uliana, A. A. et al. Ion-capture electrodialysis using multifunctional adsorptive membranes. *Science* **372**, 296–299 (2021).
21. Tan, R. et al. Hydrophilic microporous membranes for selective ion separation and flow-battery energy storage. *Nat. Mater.* **19**, 195–202 (2020).
22. Liu, Y. et al. Pillared Laminar vermiculite membranes with tunable monovalent and multivalent ion selectivity. *Adv. Mater.* **37**, e2417994 (2025).
23. Zhao, Y. et al. Self-assembled embedding of ion exchange materials into nanofiber-based hydrogel framework for fluoride capture. *Chem. Eng. J.* **431**, 134201 (2022).
24. Qiu, Y. et al. Recovery of fluoride-rich and silica-rich wastewaters as valuable resources: a resource capture ultrafiltration-bipolar membrane electrodialysis-based closed-loop process. *Environ. Sci. Technol.* **56**, 16221–16229 (2022).
25. Chang, X. et al. Selective extraction of transition metals from spent $lini_xco_ymn_{1-x-y}o_2$ cathode via regulation of coordination environment. *Angew. Chem. Int. Edit.* **61**, e202202558 (2022).
26. Ma, H. et al. Dual-channel-ion conductor membrane for low-energy lithium extraction. *Environ. Sci. Technol.* **57**, 17246–17255 (2023).
27. Wang, B. et al. Efficient separation and recovery of cobalt(II) and lithium(I) from spent lithium ion batteries (LIBs) by polymer inclusion membrane electrodialysis (PIMED). *Chem. Eng. J.* **430**, 132924 (2022).
28. Zhao, Y. et al. Formation of morphologically confined nanospaces via self-assembly of graphene and nanospheres for selective separation of lithium. *J. Mater. Chem. A* **6**, 18859–18864 (2018).
29. Zhao, Y. et al. Electric field-based ionic control of selective separation layers. *J. Mater. Chem. A* **8**, 4244–4251 (2020).
30. Yang, D. et al. Solution-processable polymer membranes with hydrophilic subnanometre pores for sustainable lithium extraction. *Nat. Water* **3**, 319–333 (2025).
31. Zuo, P. et al. Near-frictionless ion transport within triazine framework membranes. *Nature* **617**, 299–305 (2023).
32. Lu, J. et al. Efficient metal ion sieving in rectifying subnanochannels enabled by metal-organic frameworks. *Nat. Mater.* **19**, 767–774 (2020).
33. Xu, J. et al. A green and sustainable strategy toward lithium resources recycling from spent batteries. *Sci. Adv.* **8**, eabq7948 (2022).
34. Qiu, Y. et al. Investigation of fluoride and silica removal from semiconductor wastewaters with a clean coagulation-ultrafiltration process. *Chem. Eng. J.* **438**, 135562 (2022).
35. Ciez, R. E. & Whitacre, J. F. Examining different recycling processes for lithium-ion batteries. *Nat. Sustain.* **2**, 148–156 (2019).
36. Wang, J. et al. Direct recycling of spent cathode material at ambient conditions via spontaneous lithiation. *Nat. Sustain.* **7**, 1283–1293 (2024).
37. Pan, J. et al. Preparation of a monovalent selective anion exchange membrane through constructing a covalently crosslinked interface by electro-deposition of polyethyleneimine. *J. Membr. Sci.* **539**, 263–272 (2017).
38. Qiu, Y. et al. Ionic resource recovery for carbon neutral papermaking wastewater reclamation by a chemical self-sufficiency zero liquid discharge system. *Water Res.* **229**, 119451 (2023).
39. Liu, Y., Zhu, Y. & Cui, Y. Challenges and opportunities towards fast-charging battery materials. *Nat. Energy* **4**, 540–550 (2019).
40. Liu, K. et al. Ion-Ion selectivity of synthetic membranes with confined nanostructures. *ACS Nano* **18**, 21633–21650 (2024).
41. Kang, Y. et al. Nanoconfinement enabled non-covalently decorated MXene membranes for ion-sieving. *Nat. Commun.* **14**, 4075 (2023).
42. Xu, T. et al. Highly ion-permselective porous organic cage membranes with hierarchical channels. *J. Am. Chem. Soc.* **144**, 10220–10229 (2022).
43. Xu, T. et al. Perfect confinement of crown ethers in MOF membrane for complete dehydration and fast transport of monovalent ions. *Sci. Adv.* **10**, eadn0944 (2024).
44. Zhang, H. et al. Ultrafast selective transport of alkali metal ions in metal organic frameworks with subnanometer pores. *Sci. Adv.* **4**, eaaq0066 (2018).
45. Lu, J. et al. An artificial sodium-selective subnanochannel. *Sci. Adv.* **9**, eabq1369 (2023).
46. Zhang, H. et al. Angstrom-scale ion channels towards single-ion selectivity. *Chem. Soc. Rev.* **51**, 2224–2254 (2022).
47. Jiang, C. et al. Ion-"distillation" for isolating lithium from lake brine. *AIChE J* **68**, 17710 (2022).

48. Lu, G. et al. Nano-confined controllable crystallization in supramolecular polymeric membranes for ultra-selective desalination. *Nat. Commun.* **16**, 2284 (2025).

Acknowledgements

This work was supported by the Innovation and Technology Support Program Seed Application (No. ITS/332/23, Y.Z.), the RGC General Research Fund (No. 17203924, Y.Z.), and the National Natural Science Foundation (No. 22308288, Y.Z.). Y.Z. and B.V.B. acknowledge the support provided by the Fonds Wetenschappelijk Onderzoek–Vlaanderen (FWO) (No. 12A6823N and V461824N). L.X. acknowledges the support from the Fonds Wetenschappelijk Onderzoek – Vlaanderen (FWO) (No. 12B1E24N). X.Z. and S.D. acknowledge the support from the NSF Great Lakes ReNEW Water Innovation Engine (No. 2315268).

Author contributions

Y.Z. conceived and designed the experiments. Y.Z., Y.Q., and L.X. supervised the study and experiments. Y.Z., Y.Q., and L.X. conducted the membrane fabrication, characterization, and performance tests. C.Y.T. and B.V.B. provided resources for project implementation. Y.Z., Y.Q., and L.X. designed and performed the calculation. C.Y.T. and B.V.B. supported experimental results. Y.Z. wrote the paper. X.Z., S.Z., G.L., J.S., R.D., and S.D. assisted in results discussion. All the authors provided comments and revised the manuscript.

Competing interests

The authors declare no competing interests.

Additional information

Supplementary information The online version contains supplementary material available at https://doi.org/10.1038/s41467-025-67678-5.

Correspondence and requests for materials should be addressed to Yan Zhao, Bart Van der Bruggen or Chuyang Tang.

Peer review information *Nature Communications* thanks the anonymous reviewers for their contribution to the peer review of this work. A peer review file is available.

[1]Department of Civil Engineering, The University of Hong Kong, Pokfulam, Hong Kong. [2]Department of Chemical Engineering, KU Leuven, Leuven, Belgium. [3]Division of Soil and Water Management, KU Leuven, Leuven, Belgium. [4]Pritzker School of Molecular Engineering, University of Chicago, Chicago, IL, USA. [5]Chemical Sciences and Engineering Division, Argonne National Laboratory, Lemont, IL, USA. [6]Department of Chemical and Biomolecular Engineering, University of Pennsylvania, Philadelphia, PA, USA. [7]School of Energy and Environment, City University of Hong Kong, Kowloon, Hong Kong. [8]Department of Chemical Engineering, KU Leuven, Process and Environmental Technology Lab, Sint-Katelijne-Waver, Belgium. [9]Department of Engineering Science, University of Oxford, Oxford, UK. [10]Department of Chemical and Biochemical Engineering, Korea University, Seoul, Republic of Korea. [11]Nanotechnology Centre, CEET, VSB-Technical University of Ostrava, Ostrava – Poruba, Czechia. [12]These authors contributed equally: Yan Zhao, Yangbo Qiu, Lei Xia.
✉e-mail: yanzhaox@hku.hk; bart.vanderbruggen@kuleuven.be; tangc@hku.hk